Nanoscale Advances

ROYAL SOCIETY OF CHEMISTRY

PAPER

View Article Online
View Journal | View Issue

Check for updates

Cite this: *Nanoscale Adv.*, 2025, 7, 3889

Composite aerogel membranes with well dispersed nano M-TiO_2@GO for efficient photocatalysis†

Xiaozhe Zhang, ‡ Siqi Zhang,‡ Xiaohui Mao, Yifan Liu, Yaru Li, Weilong Meng, Liping Zhu * and Meifang Zhu

Received 12th March 2025
Accepted 29th April 2025

DOI: 10.1039/d5na00238a

rsc.li/nanoscale-advances

Photocatalytic technology plays a crucial role in addressing energy shortages and environmental pollution. TiO_2 has been widely applied in photocatalysis but encounters several issues, such as the easy recombination of photoexcited electrons and holes, the poor dispersion uniformity, the wide band gap, and the complex recovery process. In this work, a recyclable M-TiO_2@GO/modified chitosan composite aerogel membrane was designed and prepared for photocatalytic application, with TiO_2 nanoparticles generated by MXene oxidation (M-TiO_2) serving as the photocatalyst and modified chitosan acting as the matrix. The experimental results demonstrated that M-TiO_2 nanoparticles were *in situ* generated on the surface of graphene oxide (GO) nanosheets, forming M-TiO_2@GO nanoparticles with a 0D@2D structure. Due to the combined effects of M-TiO_2 and carbon (another product resulting from the oxidation of MXene), the band gap of M-TiO_2 nanoparticles was decreased from 3.10 eV to 2.06 eV, which significantly enhanced the photocatalytic efficiency of TiO_2. When the photocatalytic degradation performance of the aerogel membrane containing M-TiO_2@GO nanoparticles was evaluated, the sample $C_{15}M_{15}G_5$ (containing modified chitosan 15 mg/M-TiO_2 15 mg/GO 5 mg) demonstrated nearly complete degradation of Rhodamine B and Acid Blue 1 within 120 min, exhibiting excellent photocatalytic performance. In addition, the antibacterial properties of $C_{15}M_{15}G_5$ were examined and found that the antibacterial rate reached 100% following ultraviolet irradiation. In summary, this study presents an innovative strategy to obtain well-dispersed nano TiO_2, which can be used to prepare composite photocatalytic aerogel membranes with excellent catalytic performance and complete recyclability.

1. Introduction

Since TiO_2 was first discovered for water photocatalytic splitting in 1972,[1] it has drawn extensive attention due to its green, efficient, stable and reuseable features, and has been widely applied in numerous fields, such as photocatalytic hydrogen production,[2–4] CO_2 reduction,[5,6] and organic pollutant degradation,[7–9] to address the crisis of energy shortage and environmental pollution.[10] The specific surface area, uniformity, and band gap of the photocatalyst will directly influence its photocatalytic performance,[11] therefore, enhancing the porosity or dispersion, doping and hybridization can effectively enhance the photocatalytic efficiency.[12,13] However, TiO_2 still presents some issues, such as a tendency to agglomerate, difficulty in recovery, and the easy recombination of photoexcited electrons and holes.

The high surface energy of TiO_2 will lead to obvious agglomeration during the catalytic process, thereby significantly reducing the photocatalytic performance. By grafting KH570 onto the surface of TiO_2, Qin *et al.* obtained modified TiO_2 that could be evenly dispersed on the surface of the fiber.[14] However, as the photocatalytic process mainly takes place on the surface of TiO_2, the traditional surface modification technology will restrict the contact between TiO_2 and other substances, thereby influencing the photocatalytic performance of TiO_2. The *in situ* growth approach was frequently adopted to generate photocatalysts, thereby enhancing the distribution uniformity of photocatalysts. For example, Ćurković *et al.* fabricated the uniform nano-TiO_2 film through the sol–gel method, which exhibited effective photocatalytic performance (solution with 7.3 mg L^{-1} Lissamine Green B was almost completely degraded within 120 min).[15] This method leaves no substances on the surface of the catalyst and can mitigate the tendency of reduced catalytic performance. Nevertheless, the sol–gel method might sometimes yield $Ti(OH)_4$ and other precipitates, affecting the stability of the system. The *in situ* oxidation of titanium sources represented by $Ti_3C_2T_x$ MXene (such as high-temperature calcination,[16] hydrothermal method,[17] addition of an oxidizing agent,[18] *etc.*) provides

---

State Key Laboratory of Advanced Fiber Materials, College of Materials Science and Engineering, Donghua University, Shanghai 201620, China. E-mail: zhulp@dhu.edu.cn

† Electronic supplementary information (ESI) available. See DOI: https://doi.org/10.1039/d5na00238a

‡ These authors contributed equally to this work.

a solution to avoid the aforementioned problems, which is considered as an effective strategy to stably obtain nano TiO_2.

To enhance the photocatalytic activity of TiO_2, the structure of the photocatalyst is frequently regulated through the addition of a cocatalyst or doping.[19,20] The cocatalyst was often used to prevent the recombination of electrons and holes, thereby enhancing the photocatalytic efficiency of TiO_2.[21] Among them, graphene oxide (GO) is an oxidized derivative of graphene, inheriting the outstanding properties of graphene, such as excellent optical properties, mechanical flexibility, good thermal stability, and chemical stability.[22,23] Moreover, it possesses excellent hydrophilicity, enabling GO nanosheets to form a stable dispersion in water or other solvents. Additionally, the specific surface area of GO nanosheets is large, and the surface is rich in active functional groups, thus it can effectively anchor the photocatalyst to form the composite photocatalytic structure, which is currently considered as one of the most popular strategies to enhance the catalytic performance.[24–27] For example, Yang *et al.* fabricated a composite material for the efficient photocatalytic degradation of decabromodiphenyl ether (BDE209) by uniformly anchoring TiO_2 nanoparticles onto GO nanosheets. The prepared TiO_2/GO photocatalyst exhibited excellent photocatalytic performance owing to the intense coupling between GO nanosheets and TiO_2 nanoparticles. Under the optimal photocatalytic degradation conditions, the degradation efficiency of BDE209 could exceed 90%, which offered an effective approach for designing highly active catalytic materials.[28] Alternatively, by doping C, N and other elements to form heterojunctions with TiO_2, the width of the band gap can be effectively reduced and the photocatalytic activity of TiO_2 can be improved.[29] For example, Wahyuni *et al.* employed a simple hydrothermal technique to prepare N-doped TiO_2 with urea serving as the N source, and successfully decreased the band gap width from 3.20 eV to 3.06–2.96 eV.[30]

In addition, the recovery of TiO_2 is also an issue that needs to be addressed. Ding *et al.* successfully incorporated Fe_3O_4 into the photocatalyst system to facilitate the magnetic recovery of the material.[31] They synthesized a CS/Fe_3O_4/TiO_2@MXene nanocomposite photocatalyst through a one-step hydrothermal method, which exhibited excellent bacteriostatic and degradation properties. Moreover, it can be readily recycled and reused through the external magnetic field by adding Fe_3O_4. Fernández-Ibáñez *et al.* employed flocculation agents to enhance the sedimentation of colloids in a pilot plant for catalyst recovery, resulting in an impressive 97% retrieval of TiO_2.[32] However, the recycling process of TiO_2 described above is relatively complex. The preparation of composite materials of TiO_2 with polymers in the form of aerogels or membranes represents another important solution for this issue. This approach can simultaneously achieve relatively efficient photocatalysis and comprehensive recovery of TiO_2.[33–36] Chitosan (CHs), being a natural organic macromolecule, has been extensively employed as the matrix in catalytic systems for water pollutant treatment due to its environmental friendliness, easy availability, and degradability.[37–40]

To achieve high photocatalytic performance, addressing the dispersion issue, the electron–hole recombination issue and the recycling issue of TiO_2, in this study, a M-TiO_2@GO/chitosan composite aerogel membrane with a 0D@2D in 3D structure (0D M-TiO_2 nanoparticles @ 2D GO sheet dispersed in a 3D chitosan aerogel membrane) was successfully designed and fabricated. M-TiO_2 was formed *in situ* through the oxidation of MXene, which was deposited on GO nanosheets to address the aggregation issue of TiO_2. Employing GO nanosheets as the cocatalyst, which can effectively enhance the photocatalytic performance by transferring photoexcited electrons and preventing the recombination of electrons and holes. In the meantime, M-TiO_2 could form the Schottky heterojunction with carbon (another product resulting from the oxidation of MXene), effectively narrowing the band gap. The complete recovery of M-TiO_2@GO was achieved by using modified chitosan as the matrix to form a composite aerogel membrane. The excellent photocatalytic performance of M-TiO_2@GO/modified chitosan composite aerogel membranes was demonstrated through the dye degradation experiments.

2. Experimental section

2.1. Materials

Chitosan (M_W = 100 kDa, deacetylation degree 85%), LiF (99.9%) and Acid Blue 1 were purchased from Shanghai Macklin Biochemical Co. Ltd. Hydrochloric acid (HCl) solution (36.0–38.0%) and anhydrous ethanol (AR) were obtained from Sinopharm Chemical Reagent Co., Ltd. 1-(3-Dimethylaminopropyl)-3-ethylcarbodiimide (EDC, 98%) and 3,4-dihydroxyhydrocinnamic acid (HCA, 98%) were bought from TCI (Shanghai) Chemical Industry Development Co., Ltd. Ti_3AlC_2 was acquired from Jilin 11 Technology Co., Ltd. TiO_2 (99.8%, 25 nm, anatase crystal type) (P25 TiO_2) was purchased from Meryer (Shanghai) Biochemical Technology Co., Ltd. Graphene oxide (GO) dispersion (0.5–5.0 μm, 5 mg mL^{-1}) was obtained from Nanjing XFNANO Materials Tech Co., Ltd. Hydrogen peroxide was bought from Shanghai Titan Scientific Co., Ltd. Rhodamine B was acquired from Shanghai Aladdin Biochemical Technology Co., Ltd. The qualitative filter paper was bought from Hangzhou Fuyang Beimu Jiangzhi Co., Ltd. All the reagents were used as received without further purification. Deionized (DI) water with a resistance of 18 MΩ cm was prepared *via* a lab water purification system and used in all experiments.

2.2. *In situ* generation of M-TiO_2 on GO nanosheets

2.2.1. Preparation of MXene nanosheets. LiF (1.6 g) was added to 20 mL of hydrochloric acid (9 M) and stirred for 30 min. Subsequently, Ti_3AlC_2 (1.0 g) was slowly introduced into the mixture. The resulting solution underwent a constant temperature reaction at 35 °C for 36 h. Following repeated centrifugation and washing, the pH of the mixture approached a range between 5 and 6. The supernatant after centrifugation was collected and ultrasonically treated in an ice bath for 60 min to ensure the uniform dispersion of single- or few-layer MXene nanosheets, which were then frozen and freeze-dried.

2.2.2. Generation of M-TiO_2 through MXene oxidation. The corresponding mass of MXene nanosheets was uniformly

Table 1 Formulation of composite aerogel membranes

Sample	CHs-HCA (mg)	MXene (mg)	Nano-TiO_2 (mg)	GO (mg)
$C_{20}M_{10}G_5$	20	7	—	5
$C_{15}M_{15}G_5$	15	10.5	—	5
$C_{10}M_{20}G_5$	10	14	—	5
$C_{20}T_{10}G_5$	20	—	10	5
$C_{15}T_{15}G_5$	15	—	15	5
$C_{10}T_{20}G_5$	10	—	20	5

ultrasonically dispersed in 1 mL GO nanosheet dispersion solution. Then, 50 μL 30 wt% H_2O_2 solution was added, and ultrasonication was continued for 30 min to oxidize MXene into M-TiO_2 and obtain M-TiO_2@GO dispersed solution.

2.3. Preparation of aerogel membranes with TiO_2 and GO nanosheets

Modified chitosan, which is water-soluble and capable of being cross-linked, was prepared following a method modified from the literature-reported procedure.[41,42] Chitosan (0.5 g) was dissolved in dilute hydrochloric acid to obtain a 1% chitosan solution, and the pH value was adjusted to approximately 5.2. A mixture of deionized water and ethanol with a volume ratio of 1 : 1 was employed to dissolve EDC (0.36 g) and HCA (0.34 g), which were then added dropwise to the chitosan solution for the grafting reaction. The modified chitosan (CHs-HCA) was dialyzed using a dilute hydrochloric acid solution with a pH range of 4.6–4.8 as the dialysate, followed by freezing and freeze-drying.

A designed amount of CHs-HCA was dissolved in 1 mL deionized water, mixed with M-TiO_2@GO dispersion, and stirred at 60 °C. Under the influence of the residual H_2O_2 in the solution, CHs-HCA was oxidized and cross-linked. Eventually, H_2O_2 that did not take part in the oxidation reaction was decomposed under heating conditions. Subsequently, the resulting solution was cast onto a substrate membrane (qualitative filter paper), followed by freeze-drying to obtain the aerogel membrane consisting of CHs-HCA/M-TiO_2/GO (CMG), where the subscript of M represents the mass of TiO_2 generated after oxidation of MXene by theoretical calculation.

Similarly, P25 TiO_2 with a corresponding amount was uniformly dispersed along with GO nanosheets, and combined with CHs-HCA to produce the aerogel membrane consisting of CHs-HCA/TiO_2/GO (CTG) using the same method described above. The respective component masses for different samples are summarized in Table 1. And the preparation process of composite aerogel membranes is shown in Fig. 1.

2.4. Characterization

The Fourier transform infrared (FTIR) spectra of the chitosan before and after modification were recorded using a FTIR spectrophotometer (TENSOR II, BRUKER) with an ATR attachment. The grafting rate was calculated based on the integral of

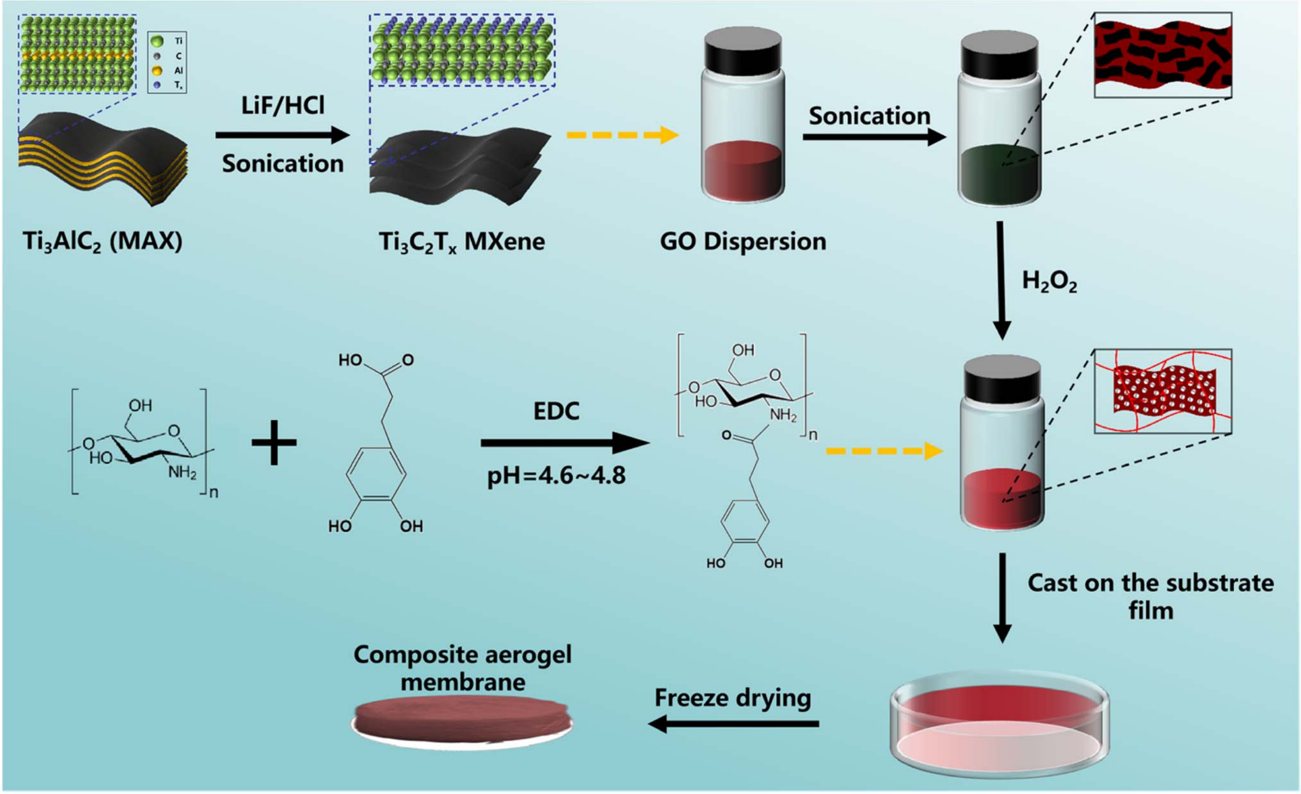

Fig. 1 Preparation process of composite aerogel membranes.

the corresponding peaks in the spectra collected from a Nuclear Magnetic Resonance (NMR) spectrometer (AVANCE NEO, BRUKER). The crystallographic structures of the MAX phase, MXene, and M-TiO_2 were determined using X-ray diffraction (XRD) (X-ray dynamic 500, Anton Paar). The samples were run at a scan rate of 5° min^{-1} over an angular (2θ) range of 3°–90°. The morphology of GO nanosheets before and after loading M-TiO_2 was characterized using a Transmission Electron Microscope (TEM) (JEM-F200, JEOL, Japan). The changes in elemental valence states in MXene before and after H_2O_2 treatment were analyzed by X-ray Photoelectron Spectroscopy (XPS) (K-Alpha, Thermo Scientific, USA). Raman spectra were obtained using an inVia-Reflex (Renishaw) with a 532 nm excitation laser. The electrical properties of M-TiO_2 in water were tested using a zeta potential analyzer (Zetasizer Nano ZS90, Malvern, UK). The micromorphology of the composite aerogel membrane was observed using a Scanning Electron Microscope (SEM) (SU8010, Hitachi, Japan). The pore size distribution of the aerogel membrane was measured by mercury intrusion porosimetry (AutoPore V 9620, Micromeritics, USA). The absorbance of the dye solution after photocatalysis was measured using an ultraviolet-visible-near infrared (UV-vis-NIR) spectrophotometer (UV-3600, SHIMADZU), and the change in concentration was calculated.

2.5. Photocatalytic performance

The composite aerogel membrane was immersed in a 100 mL, 5 ppm dye solution (Rhodamine B or Acid Blue 1) and irradiated with a 250 W ultraviolet high-pressure mercury lamp (with spectral energy centered at 365 nm) under constant temperature conditions maintained in a water bath. During this process, 5 mL aliquots of the solution were collected at 20 min intervals. UV-vis-NIR absorption spectra were recorded, and the change in dye concentration was calculated according to the principle of Lambert–Beer law, as shown in eqn (1).

$$\frac{C}{C_0} = \frac{A}{A_0} \tag{1}$$

where C_0 is the initial concentration of the dye, A_0 is the initial absorbance, C is the concentration of the dye following photocatalysis, and A is the corresponding absorbance.

In addition, the obtained photocatalytic degradation data were analyzed, and the quasi-first-order reaction kinetics was used to describe the photocatalytic degradation process of Rhodamine B or Acid Blue 1 (eqn (2)),[43] and the rate constant of the degradation reaction, k_{obs}, was obtained.

$$\ln\frac{C}{C_0} = -k_{obs} \times t \tag{2}$$

where C_0 is the initial concentration of the dye, and C is the concentration of the dye at reaction time t.

During the cycling photocatalytic performance test, the aerogel membrane after initial photocatalysis (recorded as Cycle 1) was taken out, washed with deionized water and freeze-dried. The cleaned and dried samples were tested again for photocatalysis, and the tests were recorded as Cycle x ($x = 2, 3, \ldots$).

3. Results and discussion

3.1. Preparation and characterization of M-TiO_2@GO

In this study, the dispersion of single-layer or few-layer MXene nanosheets was prepared by etching Ti_3AlC_2 in the LiF/HCl system and then freeze-dried for quantification. After the MXene and GO nanosheets were mixed and evenly dispersed, H_2O_2 was employed to oxidize the MXene attached to GO, thereby obtaining M-TiO_2@GO nanocomposite structures. Among them, the few-layer MXene was the key to achieving rapid oxidation and obtaining nano-sized TiO_2. Compared with the filtration-drying method for MXene preparation,[18] the freeze-drying method adopted in this work could effectively prevent the restacking of the few-layer MXene, enabling the acquisition of M-TiO_2 nanoparticles with smaller particle size and uniform distribution within a short time (30 min). In addition, GO nanosheets were designed as a carrier, which not only enhanced the structural stability of M-TiO_2 but also provided an effective transfer path for photoexcited electrons. Since MXene was attached and oxidized on GO, the generated M-TiO_2 could be anchored on the GO nanosheet surface, effectively avoiding the agglomeration of M-TiO_2. In the meantime, M-TiO_2 formed Schottky heterojunctions with carbon, another product resulting from the oxidation of MXene, which can effectively narrow the band gap.

A series of characterization studies of MXene before and after oxidation were performed. Based on the XRD pattern (Fig. 2a), the characteristic peak of Ti_3AlC_2 at 38.76°[44] became unobservable, whereas the peak at 9.51° associated with Ti_3AlC_2 shifted to 6.91°, which was attributed to the transformation of Ti_3AlC_2 to MXene.[45] In conjunction with the morphological changes observed in Fig. 3b and S1,† these findings suggested that single- or few-layered MXene nanosheets have been successfully synthesized. In addition, the observed diffraction peaks at 25.2°, 38.0°, 47.5°, and 62.5° corresponded to the crystallographic planes (101), (004), (200), and (204), respectively, which are characteristic of anatase TiO_2 according to PDF #21-1272.[46,47] The peaks in the Raman spectrum of oxidized MXene powders (bottom spectrum in Fig. 2b) at approximately 150, 400, 520, and 676 cm^{-1} were assigned to the E_g, B_{1g}, A_{1g} & B_{1g}, and E_g modes of anatase TiO_2,[48,49] respectively. The peaks observed at approximately 284 and 900 cm^{-1} in the Raman spectrum and 900 cm^{-1} in the FTIR spectrum (Fig. S2†) could be attributed to the oxidation of the sample induced by H_2O_2. This oxidation process resulted in the formation of oxygen-containing functional groups on the surface of the catalyst. The peak around 284 cm^{-1} corresponded to the surface hydroxyl related mode.[50,51] The peak around 900 cm^{-1} was attributed to the combination of Ti and the surrounding hydroxyl groups.[52] Ti atoms will form –TiOO groups after treatment with H_2O_2, and the peak around 900 cm^{-1} corresponded to the stretching vibration of the O_α–O_β bond.[53,54] Besides, the two broad peaks between 1200 and 1700 cm^{-1} were characteristic of the D and G modes of graphitic carbon.[55]

XPS tests of the sample (Fig. 2c and d) further elucidated the evolution of the chemical composition and structure before and

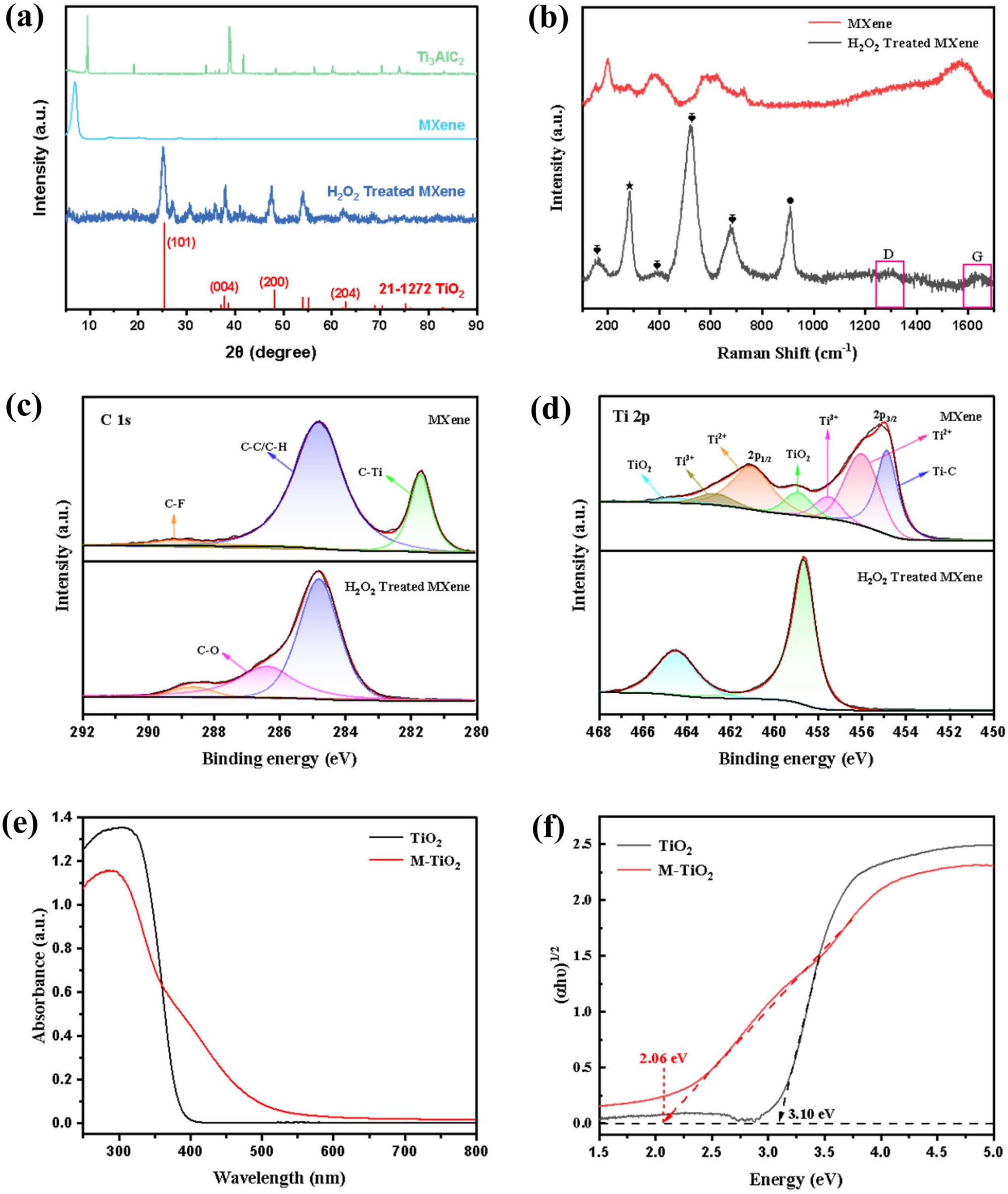

Fig. 2 Characterization of the structure and properties of M-TiO_2. (a) XRD patterns of Ti_3AlC_2, MXene and H_2O_2 treated MXene; (b) Raman spectrum; (c) high resolution XPS spectra of the C 1s region; (d) high resolution XPS spectra of the Ti 2p region of MXene before and after oxidation; (e) UV-vis DRS; (f) band-gap energy of M-TiO_2 and TiO_2 samples.

after H_2O_2 treatment. In Fig. 2c, the C 1s spectrum of MXene was deconvoluted into four peaks at binding energies of 289.2, 286.4, 284.8, and 281.7 eV, corresponding to C–F, C–O, C–C, and C–Ti bonds, respectively.[56,57] The disappearance of the C–Ti peak and the emergence of the C–O peak in MXene following H_2O_2 treatment suggested that MXene has undergone

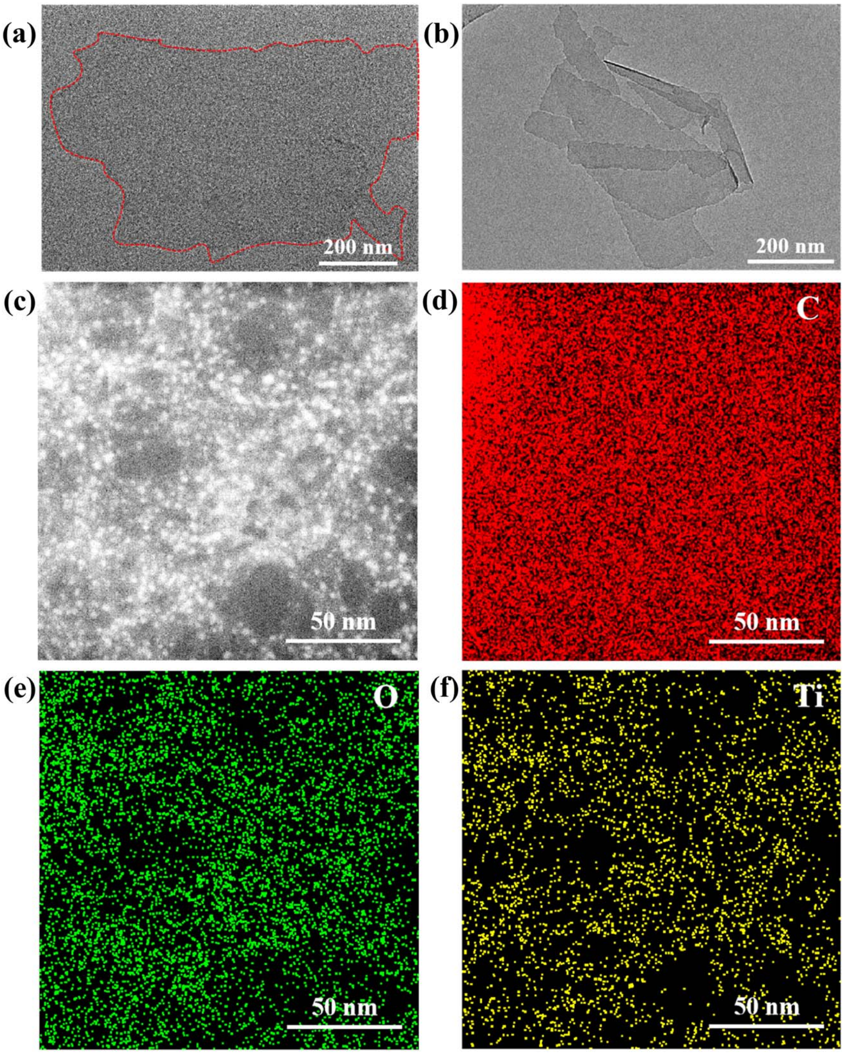

Fig. 3 Characterization of the morphology of M-TiO_2@GO. The TEM images of (a) GO, (b) MXene and (c) sample $M_{15}G_5$; EDS elemental distribution maps of (d) C, (e) O, and (f) Ti on sample $M_{15}G_5$.

a complete reaction. As illustrated in Fig. 2d and S3† (high resolution XPS spectra of the O 1s region), MXene treated with H_2O_2 exhibited only TiO_2 peaks, confirming that MXene was oxidized by H_2O_2 to form TiO_2. The above results might be due to the single-layer or few-layer structure allowing MXene to fully contact with H_2O_2, resulting in complete oxidation. The above results collectively indicated that the oxidation of MXene by H_2O_2 resulted in the formation of TiO_2 and carbon.

To investigate the photocatalytic performance of the synthesized M-TiO_2 catalyst, the corresponding characterization was conducted. Fig. 2e presents the diffuse reflectance absorption spectra of both P25 TiO_2 and the prepared M-TiO_2 samples. The bandgap absorption edges of M-TiO_2 and P25 TiO_2 were approximately 500 nm and 400 nm, respectively, indicating that both materials primarily absorbed ultraviolet light. Notably, M-TiO_2 exhibited a broader absorption spectrum, attributed to the formed carbon during the oxidation process, which reduced the recombination of photogenerated electrons in TiO_2.[58] A plot of the transformed Kubelka–Munk function *versus* light energy[59] is presented in Fig. 2f, from which the approximately determined band gaps were 2.06 and 3.10 eV for M-TiO_2 and P25 TiO_2, respectively. The main reason for the reduction of the band gap in M-TiO_2 was that during the oxidation process of MXene, carbon (C), another oxidation product, formed a Schottky heterojunction with M-TiO_2, thereby resulting in C-doped M-TiO_2.[60] The introduction of carbon atoms would create an "intermediate band" between the valence band and the conduction band of TiO_2. The existence of these intermediate bands made it easier for electrons to transit from the valence band to the conduction band, thereby effectively reducing the width of the band gap. Owing to the better dispersion and wider light absorption range, M-TiO_2 was anticipated to utilize the solar energy more effectively, thereby exhibiting superior photocatalytic performance, as will be evidenced in the photocatalytic experiment section.

Upon comparing Fig. 3a and c, it was evident that nanoparticles had uniformly formed on the lamellar structure, and the nanoparticles were thought to be TiO_2. The EDS elemental distribution maps of $M_{15}G_5$ are shown in Fig. 3c–f. The particle size distribution of the synthesized M-TiO_2 nanoparticles was characterized using a Nano Measurer, with a minimum of 30 individual particles analyzed to ensure statistical reliability. As shown in Fig. S4,† the particle size of the generated M-TiO_2 was mainly distributed within the range of 1.0–5.5 nm. Similar functional groups on the surface of GO and MXene facilitated strong hydrogen bonding, leading to intimate interfacial interactions between them, consequently, MXene could effectively disperse on the surface of GO nanosheets.[61,62] TiO_2 nanoparticles were *in situ* generated on GO nanosheets by dispersing and adsorbing MXene onto GO, resulting in the formation of 0D@2D structured M-TiO_2@GO nanoparticles. As a carrier, GO nanosheets not only enhanced the structural stability of M-TiO_2 but also provided a transfer pathway for photoexcited electrons. As an intercalation agent, M-TiO_2 produced *via* MXene oxidation significantly reduced the propensity of GO to aggregate.

3.2. Structure and morphology of CMG aerogel membranes

In order to ensure the complete recovery of M-TiO_2@GO, a composite aerogel membrane was prepared by using non-toxic, green and biocompatible modified chitosan as the matrix. Chitosan is a polymer material soluble in dilute acid, but dilute acid solutions often react with fillers and would remain in the material to affect its properties. In this section, chitosan was grafted with HCA to render it water-soluble and enhance its processability. The infrared spectrum of chitosan after grafting was presented in Fig. 4a. Notably, the high abundance of O, N, and H within the system brought abundant hydrogen bonding sites to the system, thereby causing the redshift phenomenon of the characteristic peaks of the groups.[63] The peaks at 1665, 1590, 1375, 1151, and 1025 cm^{-1} respectively corresponded to the absorption peaks of the carbonyl group (C═O), amino group (NH_2), methyl group (CH_3), C–O–C in the chitosan ring, and alcohol hydroxyl group (–OH). The peaks at 3342, 1668 and 820 cm^{-1} respectively corresponded to the absorption peaks of the O–H stretching vibration of the phenol hydroxyl group, the carboxyl group (–COOH), and the out-of-plane bending vibration of C–H in the 1,2,4-trisubstituted benzene ring in the HCA molecule. Meanwhile, the two peaks at 1442 and 1525 cm^{-1} respectively corresponded to the absorption peaks of the benzene ring skeleton. In the infrared spectrum of the prepared CHs-HCA, the peak at

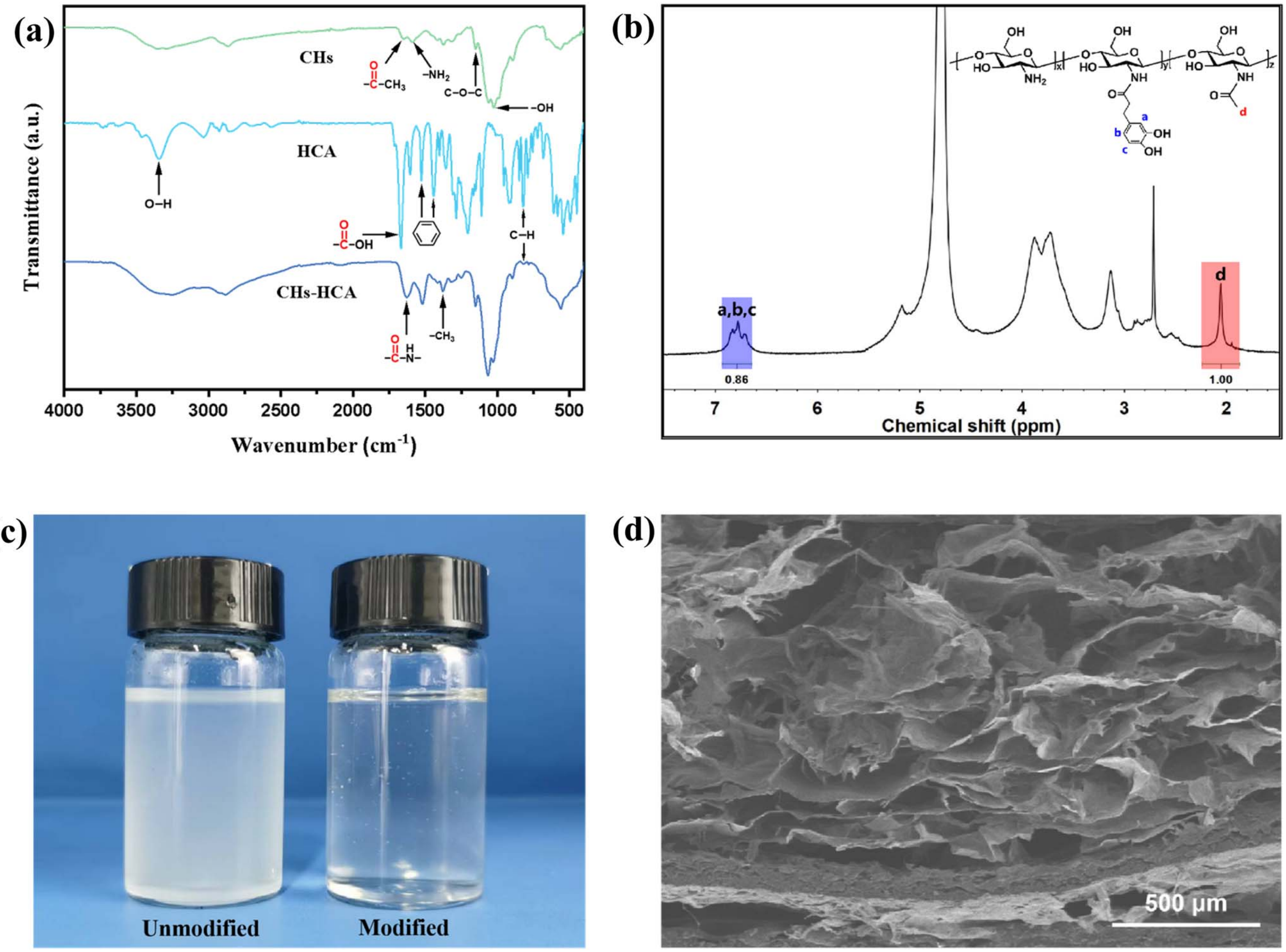

Fig. 4 Characterization of properties of CHs-HCA and the structure of the composite aerogel membrane. (a) Infrared spectrum and (b) ^{1}H-NMR of modified chitosan; (c) images of chitosan solution (left) and modified chitosan solution (right); (d) SEM image of the $C_{15}M_{15}G_5$ aerogel membrane cross-section.

1625 cm^{-1}, corresponding to the secondary amide group (–CONH-), emerged compared with chitosan, and the out-of-plane bending vibration of C–H in the 1,2,4-trisubstituted benzene ring and the absorption peak corresponding to the benzene ring skeleton appeared. Additionally, due to the substitution of the –NH_2 group in chitosan, the corresponding absorption peak transformed into the acromial peak in CHs-HCA.[64,65] These alterations demonstrated the success of the grafting reaction.

The modified chitosan was analyzed using ^{1}H-NMR spectroscopy (Fig. 4b). The grafting degree of catechol was determined by comparing the relative peak areas of the catechol groups (3H, aromatic cyclic proton, δ 6.78, D_2O) and the acetyl groups (3H, –$COCH_3$, δ 2.06, D_2O) on the chitosan backbone. The calculated grafting degree was approximately 15%. And images of the chitosan and CHs-HCA aqueous solution (Fig. 4c) demonstrated the excellent water solubility of the modified chitosan. Furthermore, a composite aerogel membrane featuring a porous structure and high specific surface area was synthesized using modified chitosan as the matrix and incorporated with $M_{15}G_5$ (as illustrated in Fig. 4d). The pore size distribution of the composite aerogel membrane was characterized using mercury intrusion porosimetry. The results indicated that the average pore size of the prepared aerogel membrane was approximately 71.5 μm, with a porosity of 93.2%, thereby confirming its significant porous structure (as shown in Fig. S5†), which was consistent with the porous morphology observed in the SEM image.

In addition, to explore the distribution of M-TiO_2@GO within the modified chitosan matrix, cross-sections of the aerogel membranes with different components were observed by SEM. The results showed that the pore wall surface of the CHs-HCA aerogel membrane was smooth. As the relative content of CHs-HCA decreased, the surface of the pore wall became rougher, and no obvious agglomeration phenomenon emerged (as shown in Fig. 5b and c). Additionally, based on the EDS scanning results, it could be observed that M-TiO_2 was evenly distributed in sample $C_{15}M_{15}G_5$ (as shown in Fig. S6†). However, when the mass of CHs-HCA was decreased to 10 mg (sample $C_{10}M_{20}G_5$), the nano-fillers agglomerated, leading to the uneven dispersion of M-TiO_2@GO and forming the obvious granular structure (as shown in the red dashed line box in Fig. 5d). The uneven distribution of the catalyst resulting from this agglomeration structure might cause the decline of the photocatalytic performance of the composite system.

3.3. Photocatalytic performance of composite aerogel membranes

The photocatalytic degradation of Rhodamine B and Acid Blue 1 was used as model reactions to evaluate the photocatalytic performance of M-TiO_2@GO/chitosan. The photocatalytic degradation performance of P25 TiO_2@GO and M-TiO_2@GO aerogel membranes was evaluated under identical conditions. Fig. 6a and b show the concentration–time curves of Rhodamine B and Acid Blue 1 degraded by different samples. UV-vis absorption spectra for the degradation of different dyes by $C_{15}M_{15}G_5$ are shown in Fig. S7.† It was observed that the composite aerogel membrane exhibited a little adsorption effect on these dyes under dark conditions, and the adsorption curve is shown in Fig. S8.† The M-TiO_2@GO composite aerogel membrane demonstrated superior photocatalytic activity compared to the P25 TiO_2@GO composite aerogel membrane. After 120 min of ultraviolet irradiation, $C_{15}T_{15}G_5$ degraded Rhodamine B by 86% and Acid Blue 1 by 72.36%, while $C_{15}M_{15}G_5$ degraded Rhodamine B by 96.03% and Acid Blue 1 by

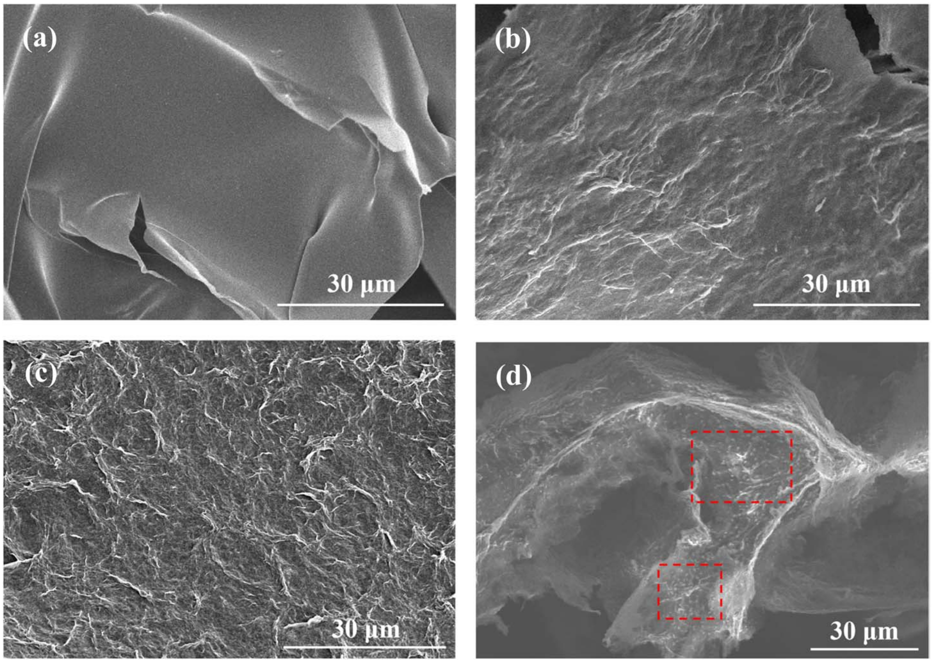

Fig. 5 Characterization of cross-section morphology of aerogel membranes with different M-TiO_2 contents. SEM images of (a) CHs-HCA, (b) $C_{20}M_{10}G_5$, (c) $C_{15}M_{15}G_5$ and (d) $C_{10}M_{20}G_5$.

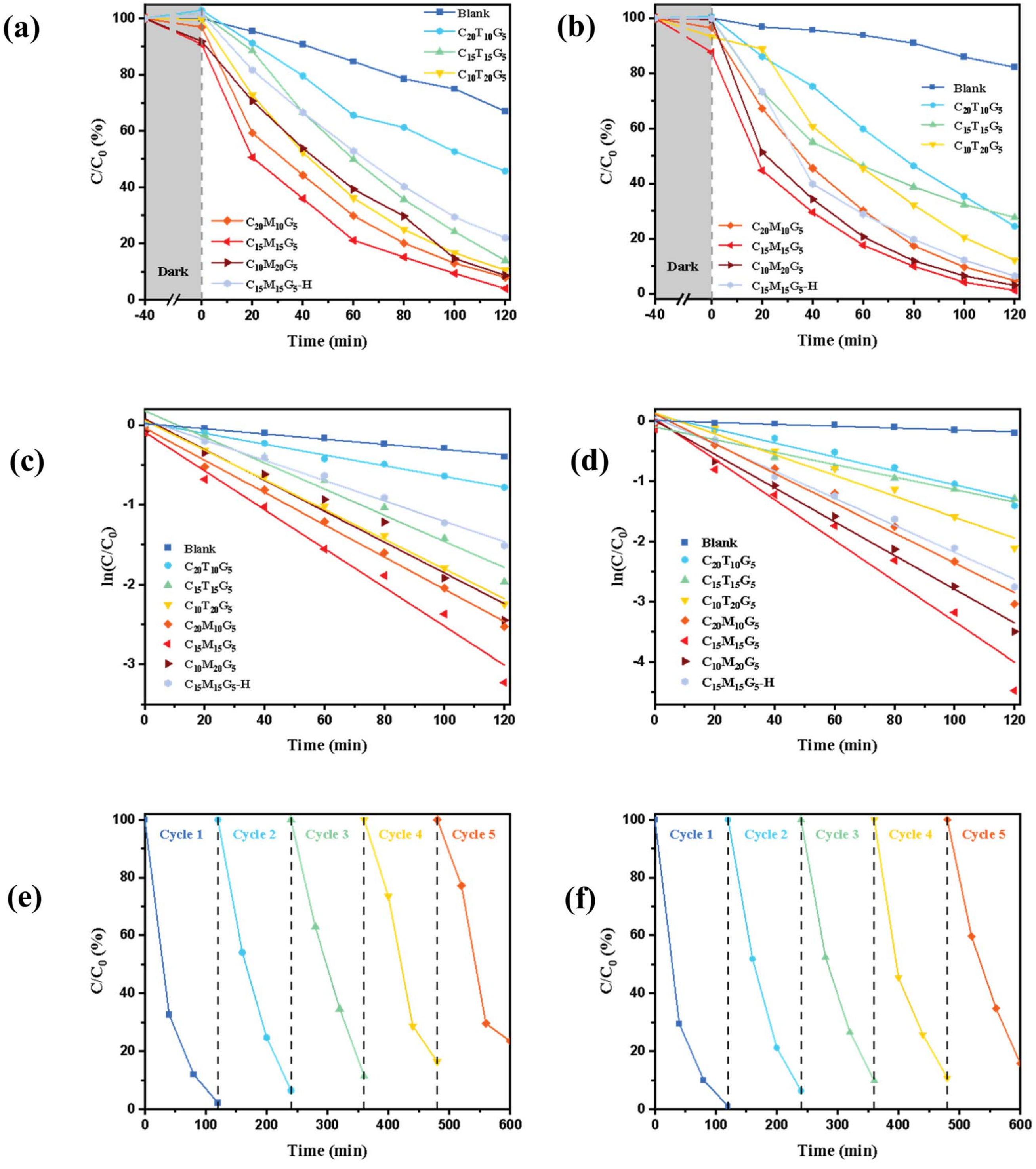

Fig. 6 Characterization of photocatalytic properties of aerogel membranes. Degradation of Rhodamine B: (a) plots of C/C_0 with time and (c) kinetic linear simulation curves using different samples, and (e) cycling performance of Rhodamine B degradation using $C_{15}M_{15}G_5$; degradation of Acid Blue 1: (b) plots of C/C_0 with time and (d) kinetic linear simulation curves using different samples, and (f) cyclic performance of Acid Blue 1 degradation using $C_{15}M_{15}G_5$.

98.86%. This could be attributed primarily to the narrower band gap of M-TiO_2 (2.06 eV), leading to enhanced catalytic degradation efficiency. Additionally, due to electrostatic interactions between MXene and GO, M-TiO_2 was synthesized *in situ* on the surface of GO during the oxidation process, ensuring intimate contact between the catalyst and co-catalyst. This configuration facilitated the transfer of excited electrons generated during catalysis and inhibited the recombination of electron–hole pairs, thereby improving the photocatalytic performance. Additionally, the dye degradation efficiency of $C_{15}M_{15}G_5$ samples prepared by heat drying in an oven (called $C_{15}M_{15}G_5$-H) was evaluated. It was observed that the dye degradation efficiency of these samples was significantly lower than that of the aerogel membrane with the same composition. After 120 min of ultraviolet irradiation, $C_{15}M_{15}G_5$-H degraded Rhodamine B by 77.94% and Acid Blue 1 by 93.62%, which was significantly lower compared to that of the $C_{15}M_{15}G_5$ sample. This discrepancy arose because the dye degradation process occurs on the surface of the catalyst TiO_2, and the porous structure (Fig. 4d) of the aerogel membrane provided a larger specific surface area, allowing for greater TiO_2 exposure and thus increasing the number of active sites and overall catalytic efficiency.

Through the quasi-first-order kinetic simulation of the degradation curves for various materials, the slope of the fitted line represents the degradation rate constant. As illustrated in Fig. 6c and d, it was evident that the chitosan aerogel membrane exhibited a strong linear relationship. Furthermore, the data indicated that sample $C_{15}M_{15}G_5$ demonstrated the highest photocatalytic reaction rate constant for both dyes: the photocatalytic reaction rate constant of Rhodamine B was 0.02433 min^{-1}, and that of Acid Blue 1 was 0.03367 min^{-1}. This enhanced performance could be attributed to the formation of a Schottky heterojunction between M-TiO_2 and carbon generated from oxidized MXene. This significantly improved the separation efficiency of photogenerated carriers and narrowed the band gap of TiO_2,[66] thereby enhancing photocatalytic efficiency.

In the field of photocatalytic technology, it was imperative to develop synthetic materials that could be efficiently recovered and reused for wastewater treatment. Fig. 6e and f illustrat the cycling performance of a composite aerogel membrane in dye degradation. Specifically, five consecutive photodegradation experiments were conducted using a $C_{15}M_{15}G_5$ aerogel membrane. Upon initial application, the degradation efficiencies for Rhodamine B and Acid Blue 1 were 97.78% and 98.86%, respectively. After five successive uses, the degradation efficiencies decreased to 76.57% for Rhodamine B and 84.31% for Acid Blue 1. Despite this reduction, the $C_{15}M_{15}G_5$ aerogel membrane retained a high level of catalytic activity, demonstrating its excellent cycling performance.

3.4. Antibacterial properties of composite aerogel membranes

In addition to organic pollutants, pathogenic bacteria are also among the pollutant components in wastewater. Based on the efficient reaction mechanism of photocatalysis technology in degrading organic pollutants, it also offers a new idea for inactivating microorganisms in wastewater. We compared the antibacterial performance of sample $C_{15}M_{15}G_5$ under dark and light conditions, as shown in Fig. 7. It can be seen that the number of colonies in the Petri dish with $C_{15}M_{15}G_5$ added under dark conditions was slightly reduced compared with that in the blank sample. This is mainly due to the electrostatic interaction between the amino groups of CHs (positively charged) with the cell membranes (negatively charged) of bacteria.[67] This interaction induces significant alterations to the cell surface, resulting in changes in permeability. This subsequently triggers osmotic imbalance and the efflux of intracellular components, ultimately leading to cell death.[68]

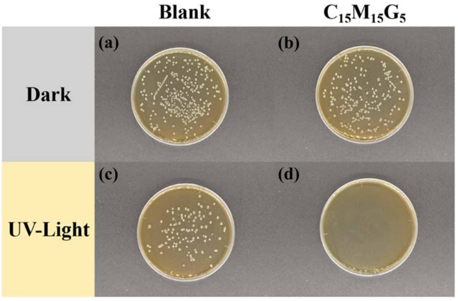

Fig. 7 Bacteriostatic properties of the samples against the colon bacillus under dark and UV-light conditions. (a) Petri dishes of the blank control group under dark conditions; (b) Petri dishes containing sample $C_{15}M_{15}G_5$ under dark conditions; (c) Petri dishes of the blank control group following UV exposure; (d) Petri dishes containing sample $C_{15}M_{15}G_5$ following UV exposure.

After ultraviolet irradiation, the number of colonies in the blank sample significantly decreased due to the bactericidal properties of ultraviolet light. However, in the culture dish containing $C_{15}M_{15}G_5$, no colonies were observed. This was primarily attributed to the fact that during irradiation, the photoelectron in the conduction band interacted with adsorbed O_2 on the surface, generating reactive oxygen species (ROS).[69] These ROS damaged bacterial cell membranes upon contact, penetrated the cells, and subsequently disrupted the protein structure or genetic material, ultimately leading to bacterial death.[67,69]

3.5. Mechanism for photocatalytic degradation of dyes and antibacterial activity by M-TiO_2@GO

Based on the aforementioned findings, we built a schematic representation of the M-TiO_2@GO catalytic degradation of dyes and sterilization, as illustrated in Fig. 8. When M-TiO_2 nanoparticles absorb ultraviolet light or visible light containing a certain energy, electrons in the valence band (VB) would be excited to transition to the conduction band (CB), forming photogenerated electrons (e^-) and leaving photogenerated holes (h^+) in the valence band,[70,71] as shown in eqn (3).

$$\text{M-TiO}_2 + h\nu \rightarrow \text{M-TiO}_2(e^-) + \text{M-TiO}_2(h^+) \qquad (3)$$

These holes could interact with water molecules on the surface of titanium dioxide to produce hydroxyl radicals ($^\bullet$OH), as shown in eqn (4). However the photogenerated electrons migrated to the GO surface and reacted with dissolved oxygen in water to form superoxide radicals ($^\bullet O_2^-$), as shown in eqn (5) and (6).

$$H_2O + \text{M-TiO}_2(h^+) \rightarrow {}^\bullet OH + H \qquad (4)$$

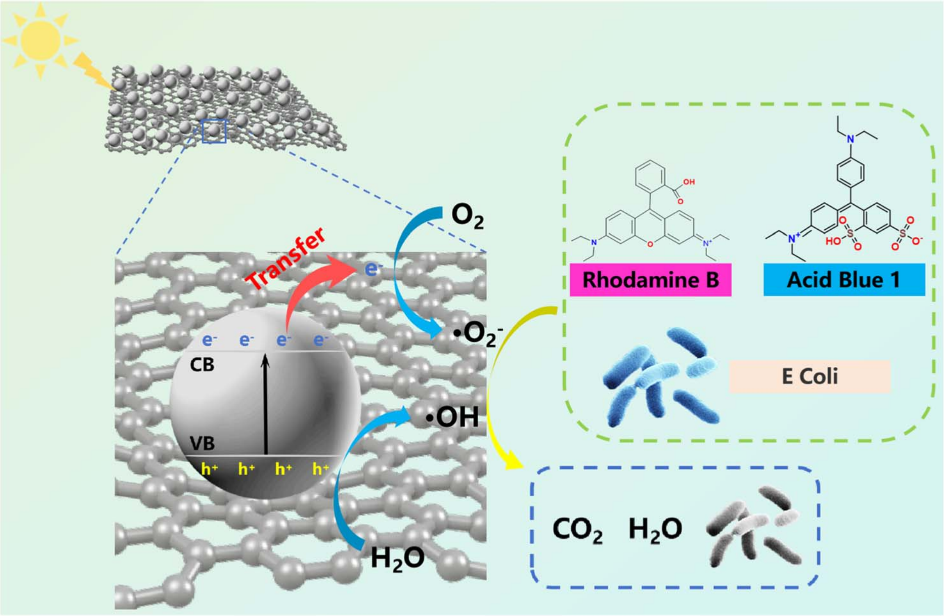

Fig. 8 Schematic illustration of the M-TiO_2@GO catalytic degradation of dyes and sterilization.

$$\text{M-TiO}_2(\text{e}^-) + \text{GO} \rightarrow \text{M-TiO}_2 + \text{GO}(\text{e}^-) \quad (5)$$

$$\text{O}_2 + \text{GO}(\text{e}^-) \rightarrow {}^{\bullet}\text{O}_2^- \quad (6)$$

Subsequently, the ROS such as $^{\bullet}OH$ and $^{\bullet}O_2^-$ exhibited strong oxidation/reduction activities. These ROS could degrade organic dyes in water into inorganic small molecules such as CO_2 and H_2O, or destroy the cell structure of bacteria, thus achieving the effect of efficient water purification.

4. Conclusion

In this study, we presented a green and rapid method for preparing well-dispersed M-TiO_2@GO photocatalysts and demonstrated that the composite aerogel membranes containing such photocatalysts exhibited excellent photocatalytic activity and recyclability. With MXene serving as the precursor of TiO_2, the *in situ* generation of TiO_2 was accomplished, effectively addressing the agglomeration issue of nano TiO_2. The two oxidation products of MXene, TiO_2 and carbon, successfully formed the Schottky heterojunction in the system, effectively reducing the band gap of TiO_2 from 3.10 eV to 2.06 eV, which resolved the relatively wide band gap problem of TiO_2 and thus significantly enhanced the photocatalytic efficiency. Additionally, GO was employed as the co-catalyst to alleviate the problem of photoexcited electron–hole recombination, and modified chitosan was prepared and used as a carrier to overcome the cumbersome issue of TiO_2 recovery. When the fabricated M-TiO_2@GO/chitosan composite aerogel membranes with a 0D@2D in 3D structure were applied to the dye degradation, after 120 min of ultraviolet light irradiation, the degradation rate of Rhodamine B reached 96.03%, and the degradation rate of Acid Blue 1 reached 98.86%. The composite membranes retained the ability to degrade 80% of the dye after five cycles. Moreover, after being exposed to ultraviolet light, the antibacterial rate of $C_{15}M_{15}G_5$ reached 100%. Overall, this work provided an effective strategy for green, efficient and recyclable photocatalytic degradation of organic pollutants.

Data availability

The data supporting this article have been included as part of the ESI.†

Conflicts of interest

The authors declare that they have no known competing financial interests or personal relationships that could have appeared to influence the work reported in this paper.

Acknowledgements

This study was financially supported by the National Key Research and Development Program of China (2022YFB3804905, 2022YFB3804900, and 2021YFA1201300) and National Natural Science Foundation of China (U23A20585).

References

1 A. Fujishima and K. Honda, Electrochemical Photolysis of Water at a Semiconductor Electrode, *Nature*, 1972, **238**(5358), 37–38.

2 J. Yang, W. Yu, C. Li, *et al.*, PtO nanodots promoting Ti_3C_2 MXene in-situ converted Ti_3C_2/TiO_2 composites for photocatalytic hydrogen production, *Chem. Eng. J.*, 2021, **420**, 129695.

3 S. Escobedo and H. de Lasa, Synthesis and Performance of Photocatalysts for Photocatalytic Hydrogen Production: Future Perspectives, *Catalysts*, 2021, **11**, 1505.

4 F. Bhom and Y. M. Isa, Photocatalytic Hydrogen Production Using TiO_2-based Catalysts: A Review, *Global Challenges*, 2024, **8**(11), 2400134.

5 J. Shen, Z. Wu, C. Li, *et al.*, Emerging applications of MXene materials in CO_2 photocatalysis, *FlatChem*, 2021, **28**, 100252.

6 F. Wang, Z. Lu, H. Guo, *et al.*, Frontispiece: Plasmonic Photocatalysis for CO_2 Reduction: Advances, Understanding and Possibilities, *Chem.–Eur. J.*, 2023, **29**(25), e202382561.

7 H. Zhang, Y. Wan, J. Luo, *et al.*, Drawing on Membrane Photocatalysis for Fouling Mitigation, *ACS Appl. Mater. Interfaces*, 2021, **13**(13), 14844–14865.

8 Z. Dong, Z. Zhang, Z. Li, *et al.*, 3D structure aerogels constructed by reduced graphene oxide and hollow TiO_2 spheres for efficient visible-light-driven photoreduction of U(VI) in air-equilibrated wastewater, *Environ. Sci.: Nano*, 2021, **8**(8), 2372–2385.

9 S. Nouacer and R. Djellabi, Easy-handling semi-floating TiO_2-based aerogel for solar photocatalytic water depollution, *Environ. Sci. Pollut. Res.*, 2023, **30**(9), 22388–22395.

10 G. Cheng, X. Liu and J. Xiong, Recent advances in coupling pollutants degradation with hydrogen production by semiconductor photocatalysis, *Chem. Eng. J.*, 2024, **501**, 157491.

11 X. Qiu, Y. Zhang, Y. Zhu, *et al.*, Applications of Nanomaterials in Asymmetric Photocatalysis: Recent Progress, Challenges, and Opportunities, *Adv. Mater.*, 2021, **33**(6), 2001731.

12 J. Pei, H. Li, D. Yu, *et al.*, g-C_3N_4-Based Heterojunction for Enhanced Photocatalytic Performance: A Review of Fabrications, Applications, and Perspectives, *Catalysts*, 2024, **14**(11), 825.

13 Y. Liu, H. Wu and Q. Wang, Strategies to improve the photocatalytic performance of covalent triazine frameworks, *J. Mater. Chem. A*, 2023, **11**(40), 21470–21497.

14 X. Qin, X. Feng, T. Zhu, *et al.*, Preparation and application of heterojunction KH570-TiO_2/MXene/PAN membranes with photocatalytic degradation and photothermal conversion properties, *J. Solid State Chem.*, 2022, **312**, 123142.

15 L. Ćurković, D. Ljubas, S. Šegota, *et al.*, Photocatalytic degradation of Lissamine Green B dye by using nanostructured sol–gel TiO_2 films, *J. Alloys Compd.*, 2014, **604**, 309–316.

16 L. Guo, Y. Liu, Q. Zeng, *et al.*, A self-driven solar coupling system with TiO_2@MXene cathode for effectively eliminating uranium and organics from complex wastewater accompanying with electricity generation, *J. Hazard. Mater.*, 2024, **465**, 133415.

17 Z. Zhuo, X. Wang, C. Shen, *et al.*, Construction of TiO_2/$SrTiO_3$ Heterojunction Derived from Monolayer Ti_3C_2 MXene for Efficient Photocatalytic Overall Water Splitting, *Chem.–Eur. J.*, 2023, **29**(12), e202203450.

18 R. Han and P. Wu, High-performance graphene oxide nanofiltration membrane with continuous nanochannels prepared by the *in situ* oxidation of MXene, *J. Mater. Chem. A*, 2019, **7**(11), 6475–6481.

19 M. Mohsin, I. A. Bhatti, M. Zeshan, *et al.*, Prospects, challenges, and opportunities of the metals-modified TiO_2 based photocatalysts for hydrogen generation under solar light irradiation: a review, *FlatChem*, 2023, **42**, 100547.

20 K. Wang, K. Yoshiiri, L. Rosa, *et al.*, TiO_2/Au/TiO_2 plasmonic photocatalyst with enhanced photocatalytic activity and stability under visible-light irradiation, *Catal. Today*, 2022, **397–399**, 257–264.

21 C. Ding, X. Qin, Y. Tian, *et al.*, PES membrane surface modification *via* layer-by-layer self-assembly of GO@TiO_2 for improved photocatalytic performance, *J. Membr. Sci.*, 2022, **659**, 120789.

22 X. Huang, X. Qi, F. Boey, *et al.*, Graphene-based composites, *Chem. Soc. Rev.*, 2012, **41**(2), 666–686.

23 R. Yang, Y. Fan, J. Hu, *et al.*, Photocatalysis with atomically thin sheets, *Chem. Soc. Rev.*, 2023, **52**(22), 7687–7706.

24 N. Thi Quynh Anh, H. M. Ngoc, N. Van Noi, *et al.*, Enhanced photocatalytic degradation of direct blue 71 dye using TiO_2-PAA-GO composite in aqueous solution, *Mater. Res. Express*, 2023, **10**(5), 55503.

25 S. Liu, Z. Su, Y. Liu, *et al.*, Mechanism and Purification Effect of Photocatalytic Wastewater Treatment Using Graphene Oxide-Doped Titanium Dioxide Composite Nanomaterials, *Water*, 2021, **13**(14), 1915.

26 K. Jayaramulu, S. Mukherjee, D. M. Morales, *et al.*, Graphene-Based Metal–Organic Framework Hybrids for Applications in Catalysis, Environmental, and Energy Technologies, *Chem. Rev.*, 2022, **122**(24), 17241–17338.

27 X. Li, J. Yu, M. Jaroniec, *et al.*, Cocatalysts for Selective Photoreduction of CO_2 into Solar Fuels, *Chem. Rev.*, 2019, **119**(6), 3962–4179.

28 M. Yang, Y. Zou, L. Ding, *et al.*, TiO_2 nanoparticles anchored on graphene oxide nanosheets as a highly active photocatalyst for decabromodiphenyl ether degradation, *Carbon Lett.*, 2023, **33**(5), 1333–1341.

29 Y. Pan, Y. Wang, S. Wu, *et al.*, One-Pot Synthesis of Nitrogen-Doped TiO_2 with Supported Copper Nanocrystalline for Photocatalytic Environment Purification under Household White LED Lamp, *Molecules*, 2021, **26**(20), 6221.

30 E. T. Wahyuni, T. Rahmaniati, A. R. Hafidzah, *et al.*, Photocatalysis over N-Doped TiO_2 Driven by Visible Light for Pb(II) Removal from Aqueous Media, *Catalysts*, 2021, **11**(8), 945.

31 H. Ding, M. Zhang, Y. Liu, *et al.*, Synthesis of CS/Fe_3O_4/TiO_2@MXene nanocomposite photocatalyst with excellent degradation and bacteriostatic properties by one-step hydrothermal method, *Ceram. Int.*, 2024, **50**(22B), 46334–46346.

32 P. Fernández-Ibáñez, J. Blanco, S. Malato, *et al.*, Application of the colloidal stability of TiO_2 particles for recovery and reuse in solar photocatalysis, *Water Res.*, 2003, **37**(13), 3180–3188.

33 S. Y. Wu, L. Li, T. Jiang, *et al.*, Excellent self-cleaning surface achieved through the synergistic effect of superhydrophilicity and photocatalysis of PVDF-TiO_2-HAP coating, *Surf. Interfaces*, 2024, **51**, 104676.

34 M. H. Zhang, Z. B. Han, G. B. Li, *et al.*, Promoted adsorption-photocatalysis synergistic removal of contaminants *via* surface regulation by a tree-like nanofiber membrane substrate, *J. Environ. Chem. Eng.*, 2024, **12**(3), 113034.

35 Q. H. Li, M. Dong, R. Li, *et al.*, Enhancement of Cr(VI) removal efficiency *via* adsorption/photocatalysis synergy using electrospun chitosan/g-C_3N_4/TiO_2 nanofibers, *Carbohydr. Polym.*, 2021, **253**, 117200.

36 L. F. Liu, P. H. Zhang and F. L. Yang, Adsorptive removal of 2,4-DCP from water by fresh or regenerated chitosan/ACF/TiO_2 membrane, *Sep. Purif. Technol.*, 2010, **70**(3), 354–361.

37 Y. Liu, F. Wu, Y. Ding, *et al.*, Preparation and Characterization of Paclitaxel/Chitosan Nanosuspensions for Drug Delivery System and Cytotoxicity Evaluation In Vitro, *Adv. Fiber Mater.*, 2019, **1**(2), 152–162.

38 J. Yin, L. Xu and A. Ahmed, Batch Preparation and Characterization of Electrospun Porous Polylactic Acid-Based Nanofiber Membranes for Antibacterial Wound Dressing, *Adv. Fiber Mater.*, 2022, **4**(4), 832–844.

39 Q. S. Zhu, X. J. Han, C. Z. Cheng, *et al.*, Study on Dissolubility of Chitosan in Four Kinds of Imidazole-Based Ionic Liquids, *Acta Polym. Sin.*, 2011, 1173–1179.

40 Y. C. Jin, Y. Lu, L. Yu, *et al.*, Synthesis of Chitosan-*O*-Poly(Ethylene Glycol) Through Diels-Alder Reaction, *Acta Polym. Sin.*, 2013, 903–908.

41 J. H. Ryu, S. Jo, M. Koh, *et al.*, Bio-Inspired, Water-Soluble to Insoluble Self-Conversion for Flexible, Biocompatible, Transparent, Catecholamine Polysaccharide Thin Films, *Adv. Funct. Mater.*, 2014, **24**(48), 7709–7716.

42 A. R. Narkar, E. Cannon, H. Yildirim-Alicea, *et al.*, Catechol-Functionalized Chitosan: Optimized Preparation Method and Its Interaction with Mucin, *Langmuir*, 2019, **35**(48), 16013–16023.

43 X. Guo, S. Hou, J. Chen, *et al.*, Transpiration-prompted Photocatalytic Degradation of Dye Pollutant with AuNPs/PANI Based Cryogels, *Chin. J. Polym. Sci.*, 2022, **40**(10), 1141–1153.

44 P. Sarkar, K. Chatterjee, P. Pal, *et al.*, Exploring the molarity of Lithium Fluoride in minimally intensive layer delamination (MILD) method for efficient room temperature synthesis of high quality $Ti_3C_2T_x$ free-standing film, *Mater. Sci. Semicond. Process.*, 2025, **185**, 108881.

45 G. Cui, X. Sun, G. Zhang, *et al.*, Electromagnetic absorption performance of two-dimensional MXene $Ti_3C_2T_x$ exfoliated by HCl + LiF etchant with diverse etching times, *Mater. Lett.*, 2019, **252**, 8–10.

46 B. Li, D. Ji, A. K. Hamouda, *et al.*, MXene-derived TiO_2 nanosheets/rGO heterostructures for superior sodium-ion storage, *ChemPhysMater*, 2025, **4**(1), 48–55.

47 K. Chen, K. Yan, Q. Xie, *et al.*, MXene-derived C-doped TiO_2/Ti_3C_2 heterojunction as a high-performance visible-light photocatalyst, *Res. Chem. Intermed.*, 2022, **48**(11), 4443–4458.

48 J. Cai, Y. Peng, P. Hu, *et al.*, H_2O_2-assisted room temperature preparation of crystalline TiO_2 and $Ti_3C_2T_x$-derived C-doped amorphous TiO_x homojunction for photocatalytic degradation of tetracycline, *Appl. Surf. Sci.*, 2025, **680**, 161430.

49 O. D. Saliu, M. Mamo, P. Ndungu, *et al.*, Starch built TiO_2 nanoarchitecture with mixed anatase and rutile phase for high energy density supercapacitor electrode, *J. Energy Storage*, 2022, **49**, 104155.

50 C. Zhao, J. Liu, B. Li, *et al.*, Multiscale Construction of Bifunctional Electrocatalysts for Long-Lifespan Rechargeable Zinc-Air Batteries, *Adv. Funct. Mater.*, 2020, **30**(36), 2003619.

51 M. Song, K. Vijayarangamuthu, E. Han, *et al.*, Enhancement of photocatalytic disinfection of surface modified rutile TiO_2 nanocatalyst, *Korean J. Chem. Eng.*, 2016, **33**(8), 2392–2395.

52 E. M. Huseynov, R. R. Hakhiyeva and N. M. Mehdiyev, FTIR study of nanocrystalline titanium carbide (TiC) particles exposed to gamma radiation, *Solid State Commun.*, 2024, **378**, 115417.

53 M. Li, X. Yan, M. Zhu, *et al.*, Theoretical investigation on the spectroscopic properties and catalytic activities of the Ti-Hydroperoxo intermediates in titanosilicate zeolites, *Microporous Mesoporous Mater.*, 2020, **299**, 110133.

54 Y. Zhang, Y. Xin, J. Cao, *et al.*, Direct hydrothermal synthesis of Titanate Nanotubes with high selectivity for oxidative desulfurization, *J. Porous Mater.*, 2023, **30**(5), 1525–1532.

55 J. Robertson and A. C. Ferrari, Interpretation of Raman spectra of disordered and amorphous carbon, *Phys. Rev. B: Condens. Matter Mater. Phys.*, 2000, **61**(20), 14095–14107.

56 Z. Zhang, H. Fu, Z. Wang, *et al.*, Mixed-Dimensional Membranes with Double 0D@2D Structures Enable Efficient and Sustainable Water Treatment, *Adv. Sustainable Syst.*, 2024, **8**(7), 2300597.

57 C. Peng, X. Yang, Y. Li, *et al.*, Hybrids of Two-Dimensional Ti_3C_2 and TiO_2 Exposing {001} Facets toward Enhanced Photocatalytic Activity, *ACS Appl. Mater. Interfaces*, 2016, **8**(9), 6051–6060.

58 W. Gao, M. Wang, C. Ran, *et al.*, One-pot synthesis of Ag/r-GO/TiO_2 nanocomposites with high solar absorption and enhanced anti-recombination in photocatalytic applications, *Nanoscale*, 2014, **6**(10), 5498–5508.

59 C. Li, Z. Wei, Q. Lu, *et al.*, Photoelectrochemical and photo-Fenton mechanism of enhanced visible light-driven nanocatalyst synthesis of $ZnFe_2O_4$/BiOI, *Environ. Sci. Pollut. Res.*, 2022, **29**(23), 34930–34942.

60 G. Jia, Y. Wang, X. Cui, *et al.*, Highly Carbon-Doped TiO_2 Derived from MXene Boosting the Photocatalytic Hydrogen Evolution, *ACS Sustain. Chem. Eng.*, 2018, **6**(10), 13480–13486.

61 B. Li, N. Wu, Y. Yang, *et al.*, Graphene Oxide-Assisted Multiple Cross-Linking of MXene for Large-Area, High-Strength, Oxidation-Resistant, and Multifunctional Films, *Adv. Funct. Mater.*, 2023, **33**(11), 2213357.

62 X. Miao, Z. Li, S. Liu, *et al.*, Ionic bridging strengthened MXene/GO nanocomposite films with extraordinary

mechanical and tribological properties, *Appl. Surf. Sci.*, 2023, **625**, 157181.

63 B. Kordić, M. Kovačević, T. Sloboda, *et al.*, FT-IR and NIR spectroscopic investigation of hydrogen bonding in indole-ether systems, *J. Mol. Struct.*, 2017, **1144**, 159–165.

64 D. Xiang, K. Wang, F. Wang, *et al.*, Coagulopathy-independent injectable catechol-functionalized chitosan shape-memory material to treat non-compressible hemorrhage, *Carbohydr. Polym.*, 2024, **346**, 122648.

65 D. Xiang, K. Wang, F. Wang, *et al.*, Coagulopathy-independent injectable catechol-functionalized chitosan shape-memory material to treat non-compressible hemorrhage, *Carbohydr. Polym.*, 2024, **346**, 122648.

66 H. Ding, M. Zhang, Y. Liu, *et al.*, Synthesis of CS/Fe_3O_4/TiO_2@MXene nanocomposite photocatalyst with excellent degradation and bacteriostatic properties by one-step hydrothermal method, *Ceram. Int.*, 2024, **50**(22B), 46334–46346.

67 G. Tsai and W. Su, Antibacterial Activity of Shrimp Chitosan against Escherichia coli, *J. Food Prot.*, 1999, **62**(3), 239–243.

68 M. Chandrasekaran, K. D. Kim and S. C. Chun, Antibacterial Activity of Chitosan Nanoparticles: A Review, *Processes*, 2020, **8**(9), 1173.

69 X. Gu, L. Hu, Z. Fu, *et al.*, Reactive TiO_2 Nanoparticles Compatibilized PLLA/PBSU Blends: Fully Biodegradable Polymer Composites with Improved Physical, Antibacterial and Degradable Properties, *Chin. J. Polym. Sci.*, 2021, **39**(12), 1645–1656.

70 M. Pelaez, N. T. Nolan, S. C. Pillai, *et al.*, A review on the visible light active titanium dioxide photocatalysts for environmental applications, *Appl. Catal., B*, 2012, **125**, 331–349.

71 Q. Guo, C. Zhou, Z. Ma, *et al.*, Fundamentals of TiO_2 Photocatalysis: Concepts, Mechanisms, and Challenges, *Adv. Mater.*, 2019, **31**(50), 1901997.